ROYAL SOCIETY OF CHEMISTRY

EDGE ARTICLE

Design and synthesis of macrocycles with tuneable diameters and helical foldamers with customizable peripheral side chains

Saquib Farooq, Aurelien Crochet [ID] and Andreas F. M. Kilbinger [ID] *

Tubular structures with nanosized pores have shown remarkable applications in areas such as ion transport and water filtration, but their development is often hindered by challenges including low yields, limited functionalization, and poor uniformity. Herein, we present a new series of macrocycles with tuneable diameters and helical foldamers featuring customizable peripheral side chains. The macrocycles, with diameters ranging from 0.8 to 1.4 nm, were synthesized in moderate to good yields using a one-pot method. Solid-state analysis revealed that these macrocycles form nanochannels, highlighting their potential applications in areas such as molecular recognition and artificial water channels (AWCs). Additionally, we synthesized helical aromatic amide polymers with narrow dispersities *via* a living chain-growth process. Our strategy enables the incorporation of diverse functional groups, including ethers, esters, acids, and amides, on the outer surfaces of the macrocycles or synthetic nanotubes. Circular dichroism (CD) spectroscopy confirmed the helical conformations of the polymers in solution. These macrocycles and foldamers present exciting opportunities for designing bioinspired membrane channels and functional nanotubes with tuneable hydrophobicity and cavity sizes, paving the way for innovative applications in nanotechnology and materials science.

Introduction

Tubular structures are of significant interest due to their extensive range of applications like molecular recognition, ion transport and optoelectronics.[1–5] Among these, tubes with nanosized pores are particularly noteworthy due to their size similarities to naturally occurring transmembrane channels.[6,7] For instance, carbon nanotube porins (CNTPs) with diameters of 0.8 nm exhibit exceptional water transport capabilities, surpassing those of many biological channels.[8–10] However, further development of CNT pores is hindered by challenges such as difficulties in adjusting pore diameters, functionalizing the inner walls of the pores, obtaining control over the length and achieving uniform pore sizes. In contrast, molecular and supramolecular tubular structures offer distinct advantages, including easier functionalization, better processability, and adjustable cavity sizes.[11] One straightforward approach to constructing organic tubes involves the stacking of cavity-containing precursors.[7,11–15] Notable examples are the aromatic oligoamide macrocycles reported by Gong's group.[16] These macrocycles, with a non-collapsible hydrophilic cavity have been shown to transport Na^+ and K^+ ions through lipid bilayers.[16] Measurements of transmembrane currents indicate that the conductance of these macrocycles exceeds that of many

natural and synthetic ion channels.[16] The macrocycles align into nanotubes through face-to-face stacking, forming large channels. In comparison to biological ion channels, most synthetic pores reported featured hydrophilic cavities with poor ion selectivity and only a few have demonstrated evidence for water transport.[17,18] However, macrocycles with nanometer–diameter hydrophobic cavities have shown significant applications in transporting water across biological membranes.[19,20] For instance, macrocycles based on arylene ethynylene backbones, synthesized through stepwise methods, have demonstrated efficient water transport across lipid membranes.[21] Recently, Aida's group created a series of macrocycles with hydrophobic cavities and pore sizes ranging from 0.9 to 1.9 nm, achieving water permeation rates that surpass those of aquaporin AQP1.[22] However, the synthesis of these macrocycles is highly challenging and suffers from low yields.[22]

Another possibility to prepare tubular structures with better yields is *via* polymerization. Several groups have reported helical polymeric aromatic amide foldamers.[23–27] These foldamers have also shown great potential in the field of water transport. Zeng's group, for example, has engineered foldamers with aliphatic hydrophobic inner pores, resulting in ultrafast water permeation with high selectivity.[25] All reported foldamer systems are synthesized *via* step-growth polymerization with a broad distribution of chain lengths and hence helical lengths. However, the transport properties, in particular across

Department of Chemistry, University of Fribourg, Chemin du Musée 9, CH-1700 Fribourg, Switzerland. E-mail: andreas.kilbinger@unifr.ch

membranes of defined widths, are highly dependent on average molecular weight and dispersity.[24]

Here, we report a synthetic protocol that allows the synthesis of macrocycles or precisely defined helical polymers that form tube-like structures in solution, carrying functional groups on both, the outside and the inner cavity.

Results and discussion

Synthesis

We recently described three new chlorophosphonium iodide reagents that tolerate aromatic amines and rapidly convert carboxylic acids into acyl chlorides.[28,29] This allows for the chain-growth synthesis of poly(aromatic amide)s under mild conditions for a large variety of amino acid monomers. The extremely high reactivity of the **PHOS3** (chloro-tri-*o*-tolylphosphonium iodide, Fig. 2A) reagent[29] prompted us to investigate its performance in the synthesis of functional aromatic amide macrocycles and polymeric helical tubes. Six monomer structures were, therefore, designed and synthesized (Fig. 1). Their gram scale synthesis is described in detail in the SI Section (Fig. S1–S6). All monomers were fully characterized by ^{1}H NMR and ^{13}C NMR spectroscopy and high-resolution mass spectrometry (HRMS).

Monomers **1–6** are all built from two aromatic amino acids known for their strong hydrogen bond-forming capabilities.[30] 4-Amino-2,3-dimethoxy benzoic acid (always depicted on the left in Fig. 1) forms a hydrogen-bonded linear building block that is connected to a 3-amino-2-alkoxy-benzoic acid derivative, which, through hydrogen bonds, gives rise to the crescent shape. Upon oligomerization or polymerization of these monomers, the upper part (as shown in Fig. 1) will form the outside of a macrocycle or helical tube, while the lower part (as shown in Fig. 1) will form the inside, *via* the formation of the three centre hydrogen bonds that stabilize the crescent conformation.

We first investigated macrocyclization reactions using the new **PHOS3** reagent. Macrocyclization reactions were carried out similarly to polymerization reactions,[29] *i.e. via* slow addition of the monomers to a **PHOS3** and pyridine-containing solution but without the presence of a mono-amine initiator. We assumed that the amino acid monomers (**M1–M6**) would act as initiators allowing chain-growth-like propagation of oligomers which would cyclize readily when reaching the appropriate degree of oligomerization.
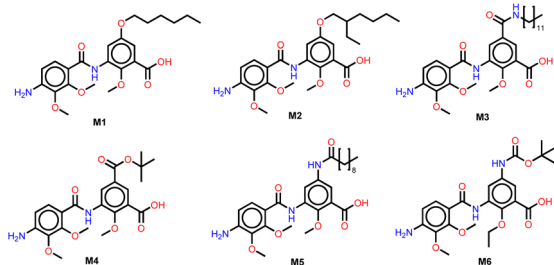
To test our hypothesis, a chloroform (CHCl$_3$) solution of monomer **M1** was added slowly (0.1 mL h^{-1}) to a chloroform mixture containing **PHOS3** and pyridine at room temperature (Fig. 2A). After the completion of monomer addition, the crude product was concentrated and precipitated in methanol to remove pyridinium salt and phosphine oxide byproducts (Fig. S7). Matrix-assisted laser desorption ionization-time of flight (MALDI-ToF) MS analysis of the crude mixture revealed a dominant signal at $m/z = 1735.8$, corresponding to the macrocycle **1a** (Fig. 2B) [M + Na$^+$] ion (expected $m/z = 1735.76$), which consists of four residue units of **M1** (Fig. S39). Additional signals at $m/z = 2163.87$ and 2592.18 correspond to macrocycles **1b** (Fig. S40) and **1c** (Fig. S41) as their sodium adducts and with five and six residue units of **M1**, respectively (Fig. 2b). To isolate these individual macrocycles, preparative high-pressure liquid chromatography (HPLC) separation was employed. 10–20% di-ethyl ether in dichloromethane (DCM) was used as the mobile phase, and a normal phase silica gel column was used as the stationary phase to obtain pure **1a** (22%), **1b** (8%), and **1c** (1%) (Table 1, and Fig. S7) as colourless solids with an overall yield of 33%. A reduced set of peaks indicating highly symmetric structures was observed in the ^{1}H-NMR spectra of **1a, 1b**, and **1c** further confirming their cyclic structure (Fig. S71, S73, and S75). The successful formation of the macrocycles (**1a–1c**) demonstrates the folding-assisted macrocyclization process driven by the H-bonding between the oligomers, as postulated above.

Crystal structure and AFM analysis of macrocycles

To further validate the cyclic structures and gain deeper insights into their conformations, we attempted to obtain single-crystal X-ray structures. Single crystals were grown by slow diffusion of methanol into a chloroform solution of **1a**. As shown in Fig. 3A, the crystal structure of **1a** reveals a well-defined square shape enclosing a hydrophobic cavity of roughly 0.8 nm between the centroids of the internal methyl groups (Fig. S60). The methoxy groups are oriented towards the cavity, due to H-bonding interactions, causing the amide hydrogens to face inward and establish a three-centered intra-molecular hydrogen bonding pattern. Interestingly, the macrocycle **1a** has a planar backbone (Fig. 3C), which facilitates perfect face-to-face π–π stacking between the aromatic flat surfaces (Fig. 3D and S60c). The packing pattern of **1a** reveals densely packed nanochannels stabilized by large π surfaces (Fig. 3C and D).

In contrast, the crystal structure of macrocycle **1b**, obtained by slow diffusion of methanol into a chloroform solution of **1b**, shows a pentagonal shape with a cavity of roughly 1.17 nm between the centroids of the internal methyl groups (Fig. S61d). Unlike **1a**, the backbone of **1b** deviates from planarity, adopting a slightly puckered conformation possibly due to increased ring strain. A slightly higher ring strain could also be responsible for the lower yields observed during the cyclization reaction (see above).

Despite numerous attempts, we were unable to obtain the crystal structure of **1c**. To estimate the internal diameter of its cavity, we utilized an optimized structure generated with the

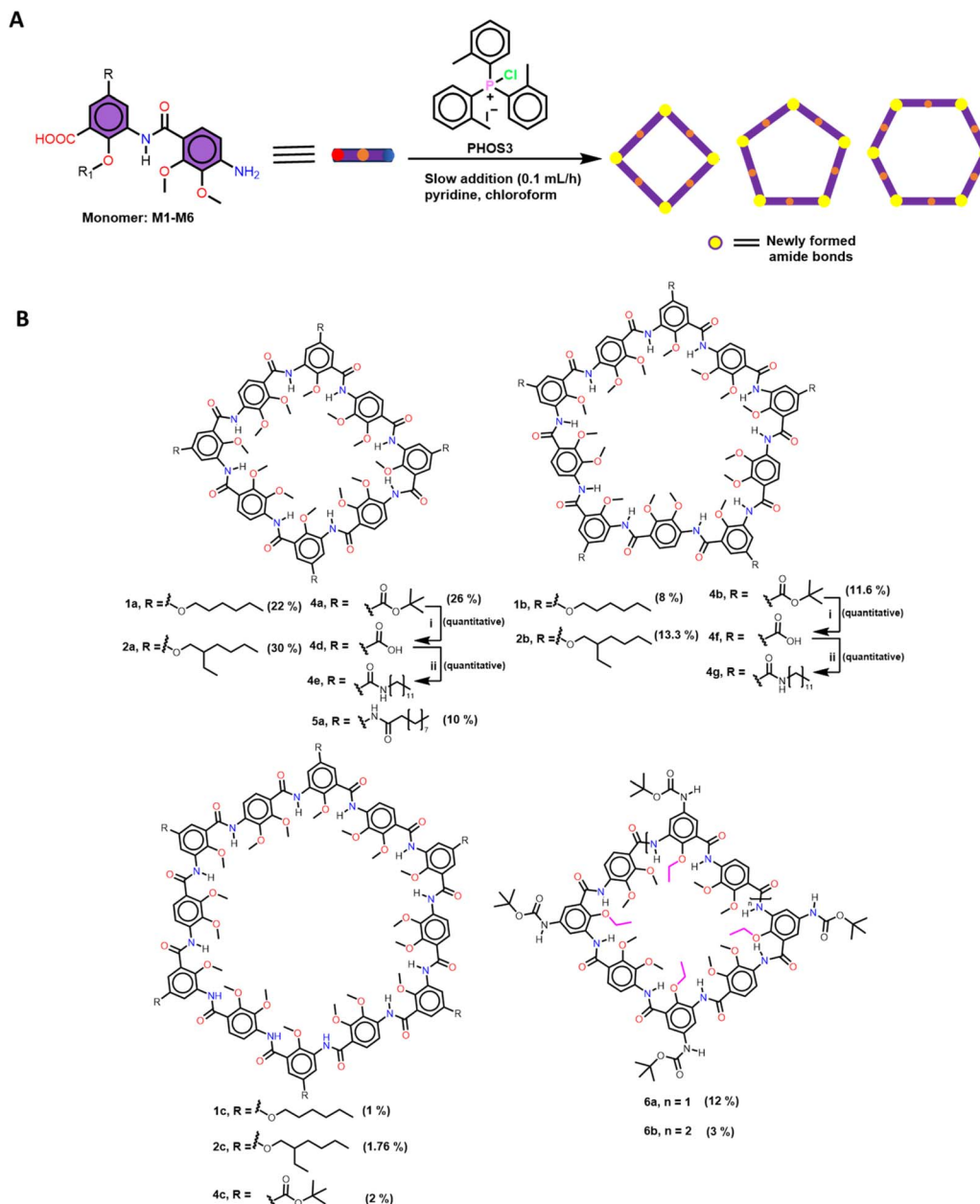**Fig. 1** Chemical structures of the different monomers synthesized in this study.

Fig. 2 Structures of macrocycles synthesized (A) synthetic route to macrocycles. (B) Molecular structures of the different macrocycles synthesized in this study. Reagents and conditions: (i) TFA, DCM, 25 °C (ii) oxalyl chloride, chloroform, dodecyl amine, pyridine, room temperature.

Spartan software (version 14), which was subsequently analyzed in the Mercury software. This analysis revealed an internal cavity diameter of 1.43 nm, measured between the centroids of the internal methyl groups (Fig. S61e).

Furthermore, the solid-state assembly of macrocycles **1a**, **1b**, and **1c** was confirmed by using atomic force microscopy (AFM). A solution (4 mg L^{-1}) of **1a**, **1b**, and **1c** drop cast from CHCl$_3$ solution onto a mica surface revealed linear fibre-like aggregates (Fig. S66–S68). These long, rod-like fibres suggest the stacking of individual macrocycles, stabilized by extensive π–π interactions, consistent with the packing patterns observed for **1a** (Fig. 3C, D) and **1b** (Fig. S61).

Preferential formation of tetramer macrocycle 1a

The efficient formation of macrocycle **1a** (Fig. 2B) can be attributed to the intrinsic preorganization of the uncyclized oligomeric backbone. Oligomers shorter than the tetramer struggle to undergo cyclization due to the rigidity of their structures, which prevents the reactive ends from coming into close proximity. In contrast, the tetramer precursor adopts a folded conformation that aligns the amine and acid chloride groups favourably, enabling rapid intramolecular cyclization. Given the irreversible nature of amide bond formation, the cyclic tetramer dominates as the primary product, while the

Table 1 Synthesized macrocycles, their isolated yields and respective monomers used for the macrocyclization

Macrocycles	Monomer	Isolated yield (%)
1a	M1	22
1b	M1	8
1c	M1	1
2a	M2	30
2b	M2	13.3
2c	M2	1.76
4a	M4	26
4b	M4	11.6
4c	M4	2
5a	M5	10
6a	M6	12
6b	M6	3

formation of higher oligomers is significantly less favoured due to deviation from planarity and an increase in ring strain (**1a** *vs.* **1b**). To support this argument, we carefully analyzed the ¹H-NMR spectra of **1a**, **1b**, and **1c** (Fig. S71, S73, and S75), which revealed significant differences in the chemical shifts of the amide protons across the three macrocycles. **1a** exhibited the most pronounced downfield shift (11.18–11.03 ppm), suggesting the presence of stronger intramolecular hydrogen bonds. This observation is consistent with the observed planar conformation of **1a**, which aligns the amide proton and methoxy oxygen atoms in the same plane for optimal hydrogen bonding interactions. In contrast, the amide proton signals for **1b** (10.52–10.46 ppm) and **1c** (10.31–10.13 ppm) appeared upfield shifted, indicating comparatively weaker hydrogen bonds, likely due to increased ring strain and deviations from

planarity. Additionally, these results also align well with Aida's reported macrocycle systems.[22] These findings underscore the crucial role of backbone rigidity and favourable hydrogen bonds in promoting efficient cyclization in a one-pot set-up under mild reaction conditions.

Synthesis of branched macrocycles from monomer M2

To explore the effects of structural modifications, we synthesized macrocycles using monomer **M2** (Fig. 1), which is structurally similar to **M1** but includes branched substituents. Using the same macrocyclization approach, we obtained macrocycles **2a**, **2b**, and **2c** (Fig. 2B) with an overall yield of 45% after preparative HPLC purification. The product distribution was 30% for **2a**, 13.3% for **2b**, and 1.76% for **2c** (Table 1, Fig. 2B, and S8). The increased yields are attributed to the branched alkyl substituents in **2a**, **2b**, and **2c**, which likely reduce π–π stacking interactions, thereby enhancing solubility and simplifying the purification process.

Synthesis of macrocycles with diverse functionalities

The synthesis of macrocycles with diverse functionalities such as amides, esters, acids *etc.* is crucial for expanding their application potential, particularly in the fields of supramolecular chemistry and materials science.[22,31–34] For example, Aida's group recently demonstrated that macrocycles with amide functionalities on their peripheries play a key role in the formation of 1D nanochannels, showcasing the importance of specific functional groups in achieving unique structural features and enhancing supramolecular interactions.[22] Inspired by these findings we attempted to synthesize amide-linked macrocycles using monomer **M3** (Fig. 1). However, the
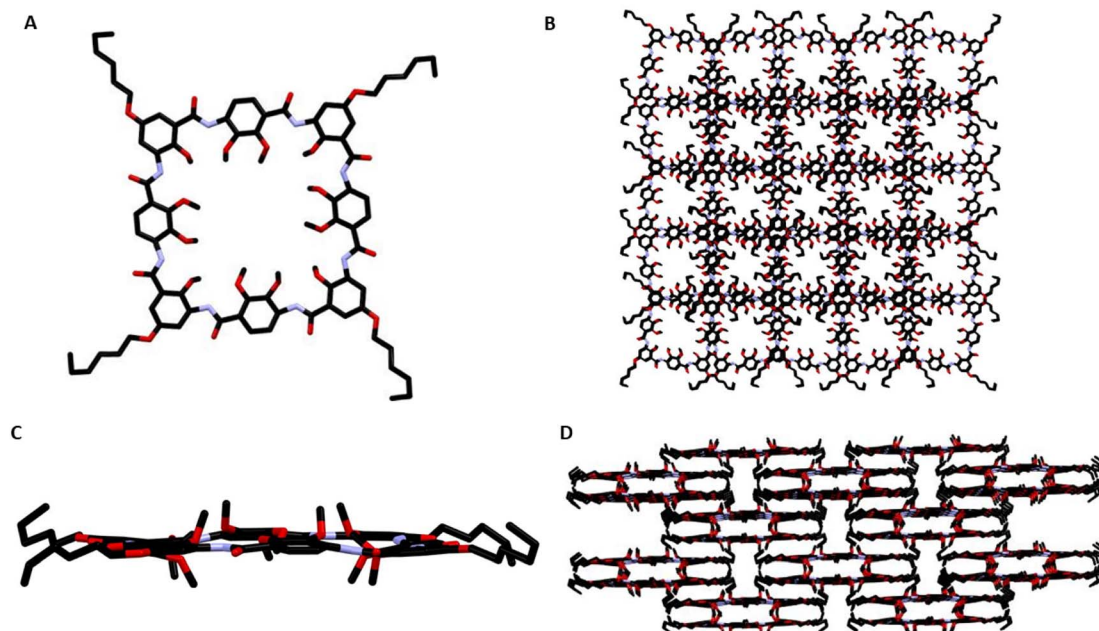

Fig. 3 X-ray crystal structures of macrocycle **1a**. (A) Top view of the crystal structure of **1a**. Atom colours carbon, black; nitrogen, blue; oxygen, red. (B) Packing structure of **1a** (top view). (C) Side view of the crystal structure of **1a**. (D) Packing structure of **1a** (side view).
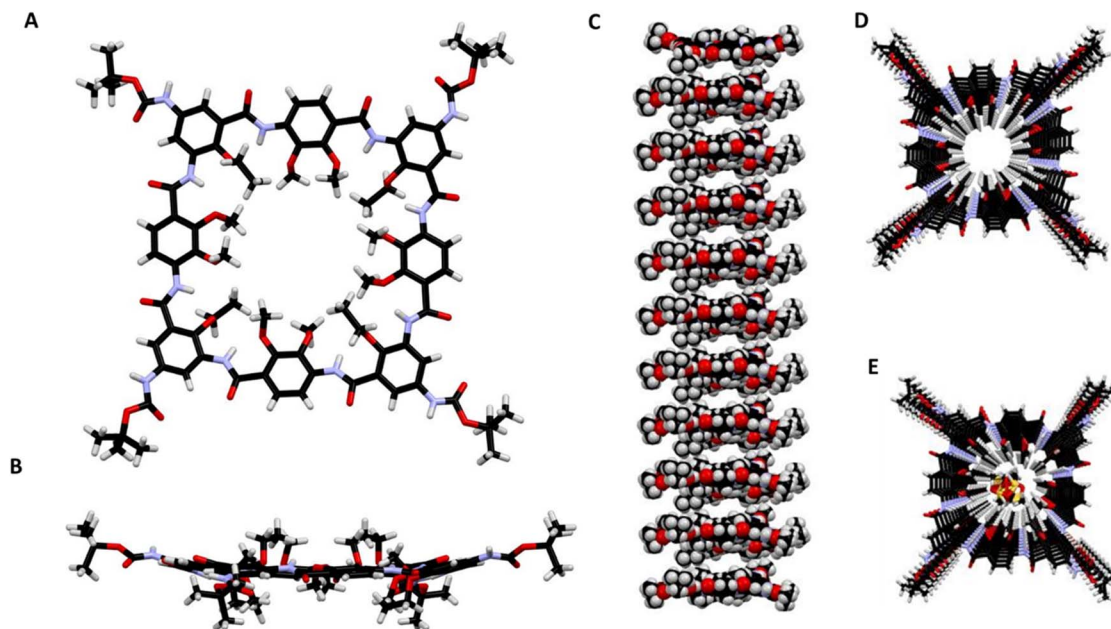
Fig. 4 Crystal structures of macrocycle **6a**. (A) Top view of the crystal structure of **6a**. Atom colours carbon, black; hydrogen, white; nitrogen, blue; oxygen, red. (B) Side view of the crystal structure of **6a**. (C) Packing structure of **6a** (side view). (D) Packing structure of **6a** (top view) with DMSO solvent masked. (E) Packing structure of **6a** (top view) with DMSO solvent in the cavity.

purification of these macrocycles proved challenging, as they could not be effectively purified using either preparative HPLC or recycling gel permeation chromatography (RGPC) with DMF as the solvent. We believe this is likely due to supramolecular aggregation caused by intermolecular hydrogen bonding of the amides.[31] To address this problem, we proposed incorporating the amide linkage as a post-functionalization reaction on a well-defined, pre-existing macrocycle. This strategy allowed us to incorporate a wide range of functionalities beyond the amide group. Therefore, we synthesized macrocycles **4a**, **4b**, and **4c** (Fig. 2B) that contain a *tert*-butyl ester group on the outer surface of the rings by utilizing monomer **M4** (Fig. 2 and Figure S9). Notably, the purification of these macrocycles was simpler using a similar procedure as described for **1a**.

The combined isolated yield was 40%, with a distribution of 26% for **4a**, 11.6% for **4b**, and 2% for **4c** (Table 1, Fig. 2B, and S9). **4a** and **4b** were fully characterized by ^{1}H NMR spectroscopy (Fig. S83 and S84) and MALDI-ToF mass spectrometry (Fig. S45 and S46) respectively. Subsequently, the *tert*-butyl groups of the purified macrocycles **4a** (Fig. 2B), and **4b** (Fig. 2B) were removed using 50% trifluoroacetic acid (TFA) in DCM to obtain the tetra carboxylic acid macrocycle **4d** (Fig. 2B), and the penta carboxylic acid macrocycle **4f** (Fig. 2B), in quantitative yields (Fig. 2B and S10, S11). The compounds **4d** and **4f** (Fig. 2B) were transformed into the corresponding acyl chlorides using excess oxalyl chloride and reacted with dodecyl amine to give the corresponding peripheral amide functional macrocycles **4e**, and **4g** (Fig. 2B, and S10, S11). The crude mixtures of **4e** and **4g** were concentrated and triturated with methanol to obtain pure macrocycles in near quantitative yield. MALDI-ToF MS analysis of the purified macrocycles revealed signals with monoisotopic masses at

$m/z = 2180.41$ for **4e**, and at $m/z = 2719.59$ for **4g** corresponding to the expected amide substituted macrocycles (Fig. S49 and S50). The post-modification or functionalization of these subnanometer-pore aramid macrocycles, in our opinion, will create new possibilities in the realm of supramolecular chemistry.

The incorporation of amide side chains, either through carbonyl (C-centered) or nitrogen (N-centered) linkages, provides a versatile approach for tuning chemical properties and enhancing intermolecular interactions in the field of supramolecular polymerization.[32] Inspired by this, we also synthesized N-centered amide-functionalized macrocycle **5a** (Fig. 2B) using monomer **M5** (Fig. 1). RGPC (in DMF) was employed to isolate **5a** with a yield of 10% (Table 1 and S12). MALDI-ToF MS analysis of the purified macrocycle **5a** revealed a signal with monoisotopic mass at $m/z = 2012.29$ corresponding to the expected $[M + Na^+]$ ion (expected $m/z = 2011.99$) (Fig. S51). However, macrocycles of larger diameters, containing five and six monomeric units of **M5** could not be effectively purified.

Tuning the hydrophobicity of macrocycle cavities has demonstrated significant applications in ion selectivity. For instance, Zeng's group illustrated that substituting a methyl group with an ethyl group increases hydrophobicity, thereby minimizing interactions with anions in artificial water channels (AWC).[25]

Motivated by these findings, we synthesized macrocycles **6a** (yield: 12%, Table 1 and Fig. 2B) and **6b** (yield: 3%, Table 1 and Fig. 2B) with enhanced hydrophobic cavities using monomer **M6** (Table 1, Fig. 2B, and S13). MALDI-ToF MS analysis of the purified macrocycles revealed signals with monoisotopic
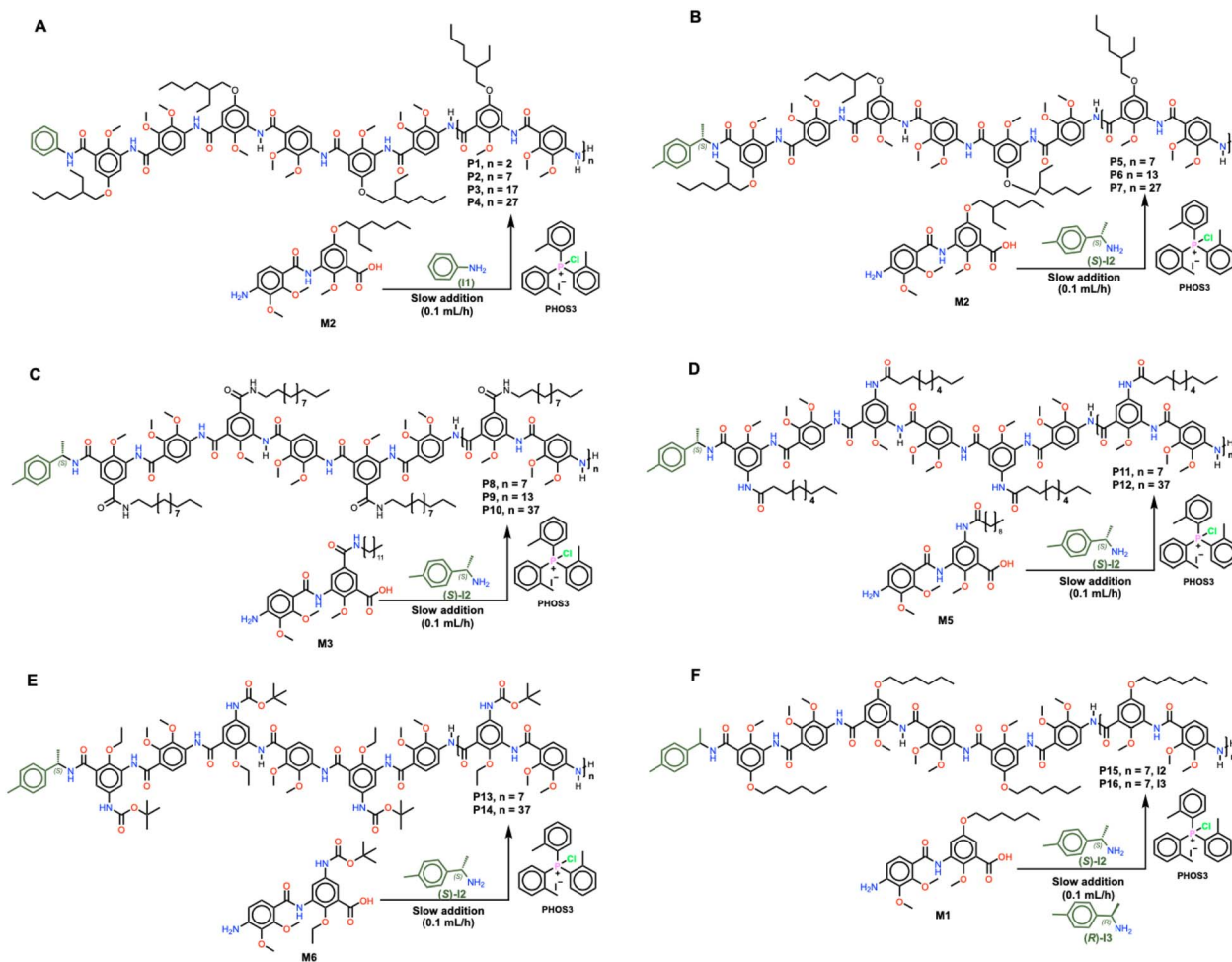
Fig. 5 Scheme of chain growth polymerization of monomers (M1–M6) under slow addition conditions and molecular structure of different polymers synthesized in this study. (A) Synthesis of polymer P1–P4 using monomer M1 and initiator I1. (B) Synthesis of polymer P5–P7 using monomer M2 and initiator (S)-I2. (C) Synthesis of polymer P8–P10 using monomer M3 and initiator (S)-I2. (D) Synthesis of polymer P11–P12 using monomer M5 and initiator (S)-I2. (E) Synthesis of polymer P13–P14 using monomer M6 and initiator (S)-I2. (F) Synthesis of polymer P15–P16 using monomer M1 and initiator (S)-I2 and (R)-I3.

masses at $m/z = 1851.76$ for **6a,** and at $m/z = 2309.00$ for **6b** corresponding to the expected $[M + Na^+]$ ion (**6a,** expected $m/z = 1851.72$) and $[M + Na^+]$ ion (**6b,** expected $m/z = 2308.91$) (Fig. S52 and S53).

To illustrate the H-bond driven folding of the self-initiated macrocyclization, we calculated (DFT, wb97xd/def2SVP, Gaussian 09 (ref. 35)) an amino acid version of **6a,** just prior to its ring-closure. The H-bond driven preorganization of the macrocycle can could clearly be observed (see SI).

Solid-state structure analysis of modified macrocycles

To evaluate the impact of amide functionality on solid-state aggregation and packing, we attempted to crystallize **4e** for single-crystal X-ray analysis, but it failed in various solvents. However, the single-crystal X-ray structure of macrocycle **6a** was successfully obtained in DMSO solution. The single-crystal X-ray structure **6a** (Fig. 4A) also reveals a well-defined square shape with a hydrophobic cavity of 0.83 nm between the centroids of the internal methyl groups and 0.9 nm between the centroids of the internal ethyl groups (Fig. S62f). The ethoxy and

methoxy groups are oriented towards the cavity, causing the amide hydrogens to face inward and establish a three-centred intramolecular hydrogen bonding pattern as observed in the case of **1a** (Fig. 4). Interestingly, **6a** forms a one-dimensional assembly in the solid-state *via* the assistance of intermolecular H-bonding between two NHBoC groups in two adjacent macrocycles (Fig. 4C). Such a perfect alignment of the cycles on top of each other resulted in the formation of an organic nanotube with well-defined hydrophobic pores (Fig. 4D).

In the crystal structure of **6a,** disordered DMSO solvent molecules were present, which were eliminated during refinement using the Platon SQUEEZE software (Table S11). This suggests that the macrocycles, particularly **4e, 4g, 5a,** and **6b** may contain internal cavities suitable for accommodating guest molecules.

Synthesis of polymers

So far, the novel amino acid monomers **M1–M6** could be shown to form macrocycles with sub-nanometer pores in reasonable yields through one-pot synthesis. Solid-state analysis revealed

that these macrocycles can self-assemble into tubular structures. Even though this approach is attractive, a key limitation is the difficulty in controlling the length of the resulting self-assembled tubes. Alternatively, these tubular structures can be made *via* step-wise organic synthesis. However, yields in solution are typically low, and solid-supported synthesis requires a large excess of valuable reagents in each coupling step. Another possible strategy to prepare tubular structures with excellent yields and good length control is living polymerization.[24,25] A narrow length distribution is critical for tailoring the properties of foldamer systems, allowing for precise control over structural features.[24] To address these challenges, a previously described chain-growth living polymerization method developed by our group was employed here to produce polymers with a wide range of helical lengths and narrow dispersities. Subsequently, **M1–M6** were polymerized by adding their monomer solutions slowly to a mixture of **PHOS3** and pyridine while using a mono-amine as an initiator (Fig. 5).

For instance, a $CHCl_3$ solution of monomer **M2** (5 equiv.) was added slowly (0.07 mL h^{-1}) to a preheated (55 °C) mixture of aniline (**I1**, 1 equiv.), **PHOS3** (15 equiv.) and pyridine (25 equiv.) (Fig. 5A and S14). After completion of monomer addition, the crude mixture was purified using RGPC (in $CHCl_3$) to obtain pure polymer **P1** which showed a narrow dispersity ($Đ = 1.08$) and a number average molecular weight ($M_{n,SEC (CHCl_3)} = 3.1$ kDa) very close to that of the [**M2**] : [**I1**] ratio ($M_{n,theo.} = 2.3$ kDa) (Table 2 and S23). Further polymerizations (Fig. 5A) were carried out by varying the monomer **M2** to initiator **I1** ratio (Table 2) to obtain polymers **P2** ($M_{n,SEC (CHCl_3)} = 6.3$ kDa, $M_{n,theo.} = 4.6$ kDa, $Đ = 1.08$), **P3** ($M_{n,SEC (CHCl_3)} = 13.0$ kDa, $M_{n,theo.} = 9.2$ kDa, $Đ = 1.16$), and **P4** ($M_{n, SEC (CHCl_3)} = 17$ kDa, $M_{n,theo.} = 13.7$ kDa, $Đ = 1.14$). All showed excellent molecular weight control while maintaining narrow dispersities (Table 2). Moreover, a plot of the observed M_n (*via* SEC) *vs.* **M2** : **I1** ratio showed a linear

relationship, supporting our claim of a living chain-growth polymerization process (Fig. 6A). Furthermore, MALDI-ToF MS analysis of the purified polymer **P2** allowed us to evaluate the defined end-groups of the living polymer chains. The mono-isotopic mass distribution of the **P2** matched with the expected polymeric structure carrying the initiator fragment (aniline) at one chain end (Fig. 6B and S54). Additionally, monomer **M2** was polymerized using a chiral primary amine (*S*)-**I2** by varying the monomer **M2** to initiator (*S*)-**I2** ratios (10 : 1, $M_{n,theo.} = 4.7$ kDa, 20 : 1, $M_{n,theo.} = 9.2$ kDa and 40 : 1, $M_{n,theo.} = 18.3$ kDa) (Tables 2 and S17, S18). The obtained polymers (Fig. 5B) **P5** ($M_{n,SEC (CHCl_3)} = 5.7$ kDa, $Đ = 1.08$), **P6** ($M_{n,SEC (CHCl_3)} = 8.7$ kDa, $Đ = 1.03$) and **P7** ($M_{n,SEC (CHCl_3)} = 15.0$ kDa, $Đ = 1.14$) showed controlled molecular weights with narrow dispersities (Table 2, and Fig. S16, S17). Drawing on the structural analysis of macrocycles derived from **M1** (which is structurally almost identical to **M2**), we can reasonably assume that the polymers synthesized above adopt a tubular or helical shape with exceptional control over their length.

Amide groups as side-chain functionalities are particularly interesting for engineering nanotube-like structures with specific, tuneable properties due to their ability to form strong hydrogen bonds. These additional interactions further increase the stability of the polymer backbone due to strong intra-molecular H-bonding between the side chains on the outer surface of the helical tube.[33] Consequently, we polymerized monomers containing amide functional groups (such as **M3** and **M5**) on the exterior using the same slow monomer addition protocol.

Therefore, **M3** was polymerized using (*S*)-**I2** as the initiator and taking the **M3** to (*S*)-**I2** ratios of 10, 20 and 40 (Fig. 3C and S18) to obtain polymers **P8** ($M_{n,theo.} = 5.5$ kDa, $M_{n,SEC (DMF)} = 6$ kDa, $Đ = 1.12$), **P9** ($M_{n,theo.} = 11.0$ kDa, $M_{n,SEC (DMF)} = 12.03$ kDa, $Đ = 1.20$) and **P10** ($M_{n,theo.} = 21.7$ kDa, $M_{n,SEC (DMF)} = 30$ kDa, $Đ$

Table 2 Number average molecular weights (M_n) and polydispersity indexes ($Đ = M_w/M_n$) of the polymers (**P1**–**P16**) synthesized from monomer **M1**–**M6** and initiator **I1**, (*S*)-**I2**, and (*R*)-**I3**

Polymer	Monomer (M)	Initiator (I)	M/I	$M_{n,theo.}$[a] [kDa]	$M_{n,SEC}$[b] [kDa]	$Đ$
P1	**M2**	**I1**	5	2.3	3.1	1.08
P2	**M2**	**I1**	10	4.6	6.3	1.08
P3	**M2**	**I1**	20	9.2	13.0	1.16
P4	**M2**	**I1**	30	13.7	17.0	1.14
P5	**M2**	(*S*)-**I2**	10	4.6	5.7	1.08
P6	**M2**	(*S*)-**I2**	20	9.2	8.7	1.03
P7	**M2**	(*S*)-**I2**	40	18.3	15.0	1.14
P8	**M3**	(*S*)-**I2**	10	5.5	6.0	1.12
P9	**M3**	(*S*)-**I2**	20	11.0	12.0	1.20
P10	**M3**	(*S*)-**I2**	40	21.7	30.0	1.20
P11	**M5**	(*S*)-**I2**	10	5.1	6.7	1.13
P12	**M5**	(*S*)-**I2**	40	20.0	16.6	1.25
P13	**M6**	(*S*)-**I2**	10	4.5	4.3	1.19
P14	**M6**	(*S*)-**I2**	40	17.8	10.5	1.17
P15	**M1**	(*R*)-**I3**	10	4.4	5.4	1.05
P16	**M1**	(*S*)-**I2**	10	4.4	6.0	1.05

[a] Theoretical molecular weight as calculated by the ratio of M/I ratio. [b] for polymers **P1**–**P7**, M_n was determined by SEC in $CHCl_3$ and for **P8**–**P16** in DMF.
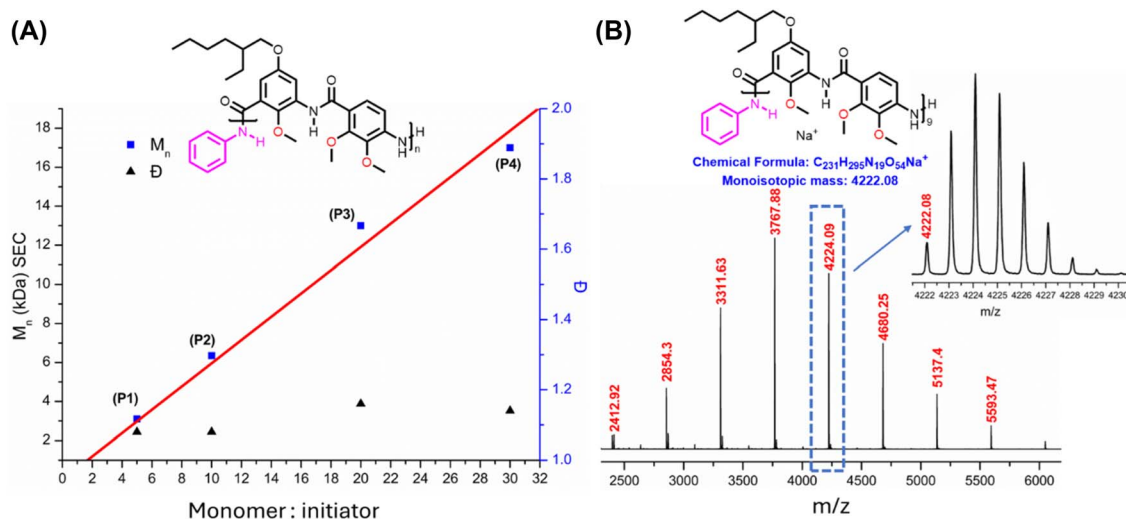
Fig. 6 (A) Linear plot of observed M_n vs. M2 : I1 ratio for the synthesis of polymers P1 to P4. (B) MALDI-ToF mass spectrum (DCTB, NaTFA) of P2 matching with the proposed end groups.

= 1.20). The excellent control over the polymerization was further realized by the end-group analysis on P8 using MALDI-ToF MS (Fig. S55).

To switch amide connectivity (N-centred) on the peripheries of the polymers, monomer M5 (Fig. 5D) was next employed in our polymerization initiated by (S)-I2 (Fig. 5D and S20). The synthesized polymers P11 ($M_{n,theo.}$ = 5.1 kDa, $M_{n\text{-SEC (DMF)}}$ = 6.75 kDa, Đ = 1.13) and P12 ($M_{n,theo.}$ = 20.0 kDa, $M_{n,SEC (DMF)}$ = 16.60 kDa, Đ = 1.25) showed narrow dispersities and M_n close to the target set by the [M5] : [(S)-I2] ratio (Table 2). Additionally, the MALDI-ToF MS analysis of polymer P11 was in very good agreement with the proposed structure (Fig. S56).

Synthesis of polymers with protective groups

Incorporating protective groups into polymeric nanotubes is an effective strategy to enhance functionality and enable further modifications. To achieve this, monomer M6 was used in our polymerization protocol. The polymerizations were initiated with (S)-I2 using M6 to (S)-I2 ratios of 10 and 40. The obtained polymer P13 ($M_{n\text{-SEC (DMF)}}$ = 4.30 kDa, Đ = 1.19) (Fig. 5E, Table 2) showed a narrow dispersity and M_n close to the theoretical mass ($M_{n,theo.}$ = 4.5 kDa, Table 2). On the other hand, P14 ($M_{n\text{-SEC (DMF)}}$ = 10.5 kDa, Đ = 1.17) while also giving a narrow dispersity, showed a molecular weight that was lower than the target value ($M_{n,theo.}$ = 17.8 kDa). We believe that this discrepancy at a higher degrees of polymerization (DP = 40) might be due to decreased solubility.

A distinct advantage of incorporating BOC groups in P13 and P14 (Fig. 5E, top middle) is the potential for post-synthetic modification to obtain amine functionalities on the aromatic moieties which potentially offer reactive sites on the external surface of the nanotubes.

Structure elucidation of polymers

To further confirm the claimed helical/folded structures of the polymers in solution, achiral monomer M1 (Fig. 5F) was

initiated using enantiomerically pure initiators (S)-I2 (enantiomeric excess (ee) = 99.5%) and (R)-I2 (ee = 99.5%) (Fig. 5F and S22). The resulting polymers P15 ((R)-I3, $M_{n,theo.}$ = 4.4 kDa, $M_{n,SEC (CHCl_3)}$ = 5.4 kDa, Đ = 1.05, Table 2) and P16 ((S)-I2, $M_{n,SEC (CHCl_3)}$ = 6.0 kDa, Đ = 1.05, Table 2) were synthesized with a degree of polymerization (DP) of approximately ten (Table 2). MALDI-ToF MS analysis of P15 revealed monoisotopic peaks matching with the proposed chiral end group (Fig. S57). CD-spectroscopic analysis of P15 (R-enantiomer) and P16 (S-enantiomer) in toluene at room temperature showed opposing CD signals for P15 (R-enantiomer) and P16 (S-enantiomer) which highlight the enantiospecific induction of helicity (Fig. 7). This clear differentiation indicates that the helical sense of the polymer is biased by the handedness of the initiator, with each enantiomer generating a polymer with an opposite helical twist.

Furthermore, the CD results for polymer P8 (Fig. 5C), which also carries a chiral initiator, also showed a significant CD signal (Fig. S70). The consistent findings across different
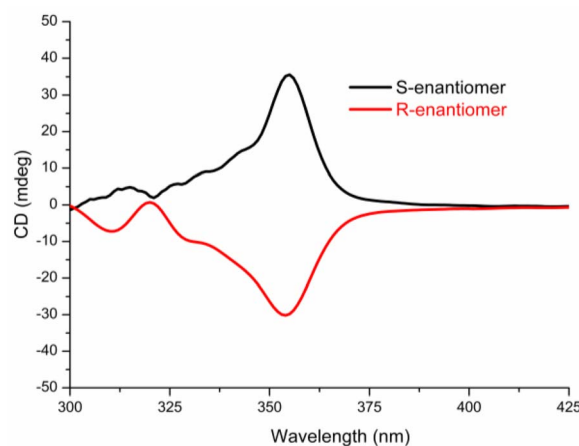

Fig. 7 CD spectra of P15 (red) and P16 (black) recorded in toluene (100 mg L⁻¹) at room temperature.

polymers reinforce the conclusion that these polymers adopt helical conformations in solution.

Conclusion

In conclusion, we report the strategic design and successful synthesis of macrocycles with clearly defined inner cavities, achieved in moderate to good yields. This synthetic design enables the functionalization of both the periphery and internal cavities. Although not explored in this study, the design framework provides the potential to incorporate other functional groups, such as chiral moieties, which could potentially be useful for future applications in asymmetric catalysis and selective recognition of chiral guest molecules. Notably, we incorporated a range of functional groups, including ethers, esters, acids, and amides, on the macrocycle periphery.

Single crystal X-ray analysis of several macrocycles revealed the formation of nanotubes with hydrophobic cavities ranging from 0.8 nm to 1.4 nm, suggesting potential applications as artificial water channels (AWC), functional supramolecular polymers, and in molecular recognition, as demonstrated by research from our group,[36] Aida,[22] Meijer,[34,37] Zeng,[25] and Manish's groups.[19,20]

Additionally, we showed that helical polymeric foldamers with various functionalities can be prepared in good yields *via* a chain-growth living polymerization method giving good control over the helical lengths and dispersities. The high yield of tetrameric macrocycles under self-condensation conditions indicates that four monomeric units are required per helical turn. Notably, circular dichroism (CD) measurements confirm the helical conformations of the polymers in solution. We believe these foldamers will pave the way for designing functional nanotubes.

Author contributions

S. F. and A. F. M. K. conceived the idea. S. F. synthesized all monomers, macrocycles, and polymers, conducted molecular and polymer analyses, and crystallised all the macrocycles. A. C. measures the crystal structure of **M1**. All the authors reviewed the manuscript.

Conflicts of interest

The authors declare no competing interests.

Data availability

The data supporting this article have been included as part of the supplementary information (SI). Supplementary information on monomer synthesis, macrocycle and polymer synthesis, SEC, MALDI ToF MS, AFM, CD, NMR and HRMS analysis is available. See DOI: **https://doi.org/10.1039/d5sc04138d**.

CCDC 2424442 and 2424464–2424466 contain the supplementary crystallographic data for this paper.[38a–d]

Acknowledgements

References

1 A. Harada, J. Li and M. Kamachi, *Nature*, 1993, **364**, 516–518.
2 S. Samitsu, J. Araki, T. Shimomura and K. Ito, *Macromolecules*, 2008, **41**, 5385–5392.
3 T. Ikeda, T. Ooya and N. Yui, *Macromol. Rapid Commun.*, 2000, **21**, 1257–1262.
4 L. S. Shimizu, S. R. Salpage and A. A. Korous, *Acc. Chem. Res.*, 2014, **47**, 2116–2127.
5 M. Aoyagi, K. Biradha and M. Fujita, *J. Am. Chem. Soc.*, 1999, **121**, 7457–7458.
6 B. H. Hong, S. C. Bae, C. W. Lee, S. Jeong and K. S. Kim, *Science*, 2001, **294**, 348–351.
7 D. T. Bong, T. D. Clark, J. R. Granja and M. Reza Ghadiri, *Angew. Chem., Int. Ed.*, 2001, **40**, 988–1011.
8 R. H. Tunuguntla, R. Y. Henley, Y.-C. Yao, T. A. Pham, M. Wanunu and A. Noy, *Science*, 2017, **357**, 792–796.
9 B. Hinds, *Curr. Opin. Solid State Mater. Sci.*, 2012, **16**, 1–9.
10 R. B. Schoch, J. Han and P. Renaud, *Rev. Mod. Phys.*, 2008, **80**, 839–883.
11 C. Z. Liu, M. Yan, H. Wang, D. W. Zhang and Z. T. Li, *ACS Omega*, 2018, **3**, 5165–5176.
12 B. Gong and Z. Shao, *Acc. Chem. Res.*, 2013, **46**, 2856–2866.
13 K. Yamato, M. Kline and B. Gong, *Chem. Commun.*, 2012, **48**, 12142–12158.
14 P. D. Frischmann, B. J. Sahli, S. Guieu, B. O. Patrick and M. J. MacLachlan, *Chem.–Eur. J.*, 2012, **18**, 13712–13721.
15 G. Gattuso, S. Menzer, S. A. Nepogodiev, J. F. Stoddart and D. J. Williams, *Angew. Chem., Int. Ed.*, 1997, **36**, 1451–1454.
16 A. J. Helsel, A. L. Brown, K. Yamato, W. Feng, L. Yuan, A. J. Clements, S. V. Harding, G. Szabo, Z. Shao and B. Gong, *J. Am. Chem. Soc.*, 2008, **130**, 15784–15785.
17 M. S. Kaucher, M. Peterca, A. E. Dulcey, A. J. Kim, S. A. Vinogradov, D. A. Hammer, P. A. Heiney and V. Percec, *J. Am. Chem. Soc.*, 2007, **129**, 11698–11699.
18 M. Engels, D. Bashford and R. M. Ghadiri, *J. Am. Chem. Soc.*, 1995, **117**, 9151–9158.
19 W. Song and M. Kumar, *Langmuir*, 2022, **38**, 9085–9091.
20 W. Song, C. Lang, Y. X. Shen and M. Kumar, *Annu. Rev. Mater. Res.*, 2018, **48**, 57–82.
21 X. Zhou, G. Liu, K. Yamato, Y. Shen, R. Cheng, X. Wei, W. Bai, Y. Gao, H. Li, Y. Liu, F. Liu, D. M. Czajkowsky, J. Wang, M. J. Dabney, Z. Cai, J. Hu, F. V. Bright, L. He, X. C. Zeng, Z. Shao and B. Gong, *Nat. Commun.*, 2012, **3**, 949.
22 Y. Itoh, S. Chen, T. Konda, T. Aoki, T. Ueda, I. Shimada, J. J. Cannon, C. Shao, J. Shiomi, K. V Tabata, H. Noji, K. Sato and T. Aida, *Science*, 2022, **376**, 738–743.

23 S. Qi, C. Zhang, T. Yan, F. Yang, J. Zhang, S. Mao and Z. Dong, *Macromol. Rapid Commun.*, 2020, **41**, 2000099.

24 J. Shen, J. Fan, R. Ye, N. Li, Y. Mu and H. Zeng, *Angew. Chem., Int. Ed.*, 2020, **59**, 13328–13334.

25 A. Roy, J. Shen, H. Joshi, W. Song, Y. M. Tu, R. Chowdhury, R. Ye, N. Li, C. Ren, M. Kumar, A. Aksimentiev and H. Zeng, *Nat. Nanotechnol.*, 2021, **16**, 911–917.

26 M. Schulze and A. F. M. Kilbinger, *J. Polym. Sci., Part A: Polym. Chem.*, 2016, **54**, 1731–1741.

27 Y. X. Lu, Z. M. Shi, Z. T. Li and Z. Guan, *Chem. Commun.*, 2010, **46**, 9019–9021.

28 S. Pal, P. T. Nguyen, A. Molliet, M. Alizadeh, A. Crochet, R. D. Ortuso and A. F. M. Kilbinger, *Nat. Chem.*, 2021, **13**, 705–713.

29 S. Pal, L. Hong, R. V. M. Freire, S. Farooq, S. Salentinig and A. F. M. Kilbinger, *Macromolecules*, 2023, **56**, 7984–7992.

30 D. W. Zhang, X. Zhao, J. L. Hou and Z. T. Li, *Chem. Rev.*, 2012, **112**, 5271–5316.

31 K. V. Rao, D. Miyajima, A. Nihonyanagi and T. Aida, *Nat. Chem.*, 2017, **9**, 1133–1139.

32 E. Weyandt, I. A. W. Filot, G. Vantomme and E. W. Meijer, *Eur. J. Org. Chem.*, 2021, **27**, 9700–9707.

33 W. Song, C. Lang, Y. X. Shen and M. Kumar, *Annu. Rev. Mater. Res.*, 2018, **48**, 57–82.

34 T. Aida, E. W. Meijer and S. I. Stupp, *Science*, 2012, **335**, 813–817.

35 M. J. Frisch, G. W. Trucks, H. B. Schlegel, G. E. Scuseria, M. A. Robb, J. R. Cheeseman, G. Scalmani, V. Barone, B. Mennucci, G. A. Petersson, H. Nakatsuji, M. Caricato, X. Li, H. P. Hratchian, A. F. Izmaylov, J. Bloino, G. Zheng, J. L. Sonnenberg, M. Hada, M. Ehara, K. Toyota, R. Fukuda, J. Hasegawa, M. Ishida, T. Nakajima, Y. Honda, O. Kitao, H. Nakai, T. Vreven, J. A. Montgomery Jr, J. E. Peralta, F. Ogliaro, M. Bearpark, J. J. Heyd, E. Brothers, K. N. Kudin, V. N. Staroverov, T. Keith, R. Kobayashi, J. Normand, K. Raghavachari, A. Rendell, J. C. Burant, S. S. Iyengar, J. Tomasi, M. Cossi, N. Rega, J. M. Millam, M. Klene, J. E. Knox, J. B. Cross, V. Bakken, C. Adamo, J. Jaramillo, R. Gomperts, R. E. Stratmann, O. Yazyev, A. J. Austin, R. Cammi, C. Pomelli, J. W. Ochterski, R. L. Martin, K. Morokuma, V. G. Zakrzewski, G. A. Voth, P. Salvador, J. J. Dannenberg, S. Dapprich, A. D. Daniels, O. Farkas, J. B. Foresman, J. V. Ortiz, J. Cioslowski and D. J. Fox, *Gaussian 09, Revision D.01*, Gaussian, Inc., Wallingford CT, 2013.

36 S. Farooq, J. A. Malla, M. Nedyalkova, R. V. M. Freire, I. Mandal, A. Crochet, S. Salentinig, M. Lattuada, C. T. McTernan and A. F. M. Kilbinger, *Angew. Chem., Int. Ed.*, 2025, e202504170.

37 T. Aida and E. W. Meijer, *Isr. J. Chem.*, 2020, **60**, 33–47.

38 (*a*) CCDC 2424442: Experimental Crystal Structure Determination, 2025, DOI: **10.5517/ccdc.csd.cc2mcttn**; (*b*) CCDC 2424464: Experimental Crystal Structure Determination, 2025, DOI: **10.5517/ccdc.csd.cc2mcvjd**; (*c*) CCDC 2424465: Experimental Crystal Structure Determination, 2025, DOI: **10.5517/ccdc.csd.cc2mcvkf**; (*d*) CCDC 2424466: Experimental Crystal Structure Determination, 2025, DOI: **10.5517/ccdc.csd.cc2mcvlg**.